



Hubble Space Telescope Observations of NGC 253 Dwarf Satellites: Three Ultra-faint Dwarf Galaxies*

Burçin Mutlu-Pakdil^{1,2}, David J. Sand³, Denija Crnojević⁴, Michael G. Jones³, Nelson Caldwell⁵, Puragra Guhathakurta⁶, Anil C. Seth⁷, Joshua D. Simon⁸, Kristine Spekkens^{9,10}, Jay Strader¹¹, and Elisa Toloba¹²

¹ Kavli Institute for Cosmological Physics, University of Chicago, Chicago, IL 60637, USA; burcinmp@uchicago.edu

² Department of Astronomy and Astrophysics, University of Chicago, Chicago, IL 60637, USA

³ Steward Observatory, University of Arizona, 933 North Cherry Avenue, Tucson, AZ 85721, USA

⁴ University of Tampa, 401 West Kennedy Boulevard, Tampa, FL 33606, USA

⁵ Center for Astrophysics, Harvard & Smithsonian, 60 Garden Street, Cambridge, MA 02138, USA

⁶ University of California Observatories/Lick Observatory, University of California, Santa Cruz, CA 95064, USA

⁷ University of Utah, 115 South 1400 East, Salt Lake City, UT 84112-0830, USA

⁸ Observatories of the Carnegie Institution for Science, 813 Santa Barbara Street, Pasadena, CA 91101, USA

⁹ Department of Physics and Space Science, Royal Military College of Canada P.O. Box 17000, Station Forces Kingston, ON, K7K 7B4, Canada

¹⁰ Department of Physics, Engineering Physics and Astronomy, Queen's University, Kingston, ON, K7L 3N6, Canada

¹¹ Department of Physics and Astronomy, Michigan State University, East Lansing, MI 48824, USA

¹² Department of Physics, University of the Pacific, 3601 Pacific Avenue, Stockton, CA 95211, USA

Received 2021 August 20; revised 2021 December 13; accepted 2021 December 15; published 2022 February 15

Abstract

We present deep Hubble Space Telescope (HST) imaging of five faint dwarf galaxies associated with the nearby spiral NGC 253 ($D \approx 3.5$ Mpc). Three of these are newly discovered dwarf galaxies, while all five were found in the Panoramic Imaging Survey of Centaurus and Sculptor, a Magellan+Megacam survey to identify faint dwarfs and other substructures in resolved stellar light around massive galaxies outside of the Local Group. Our HST data reach $\gtrsim 3$ magnitudes below the tip of the red giant branch for each dwarf, allowing us to derive their distances, structural parameters, and luminosities. All five systems contain mostly old, metal-poor stellar populations (age ~ 12 Gyr, $[M/H] \lesssim -1.5$) and have sizes ($r_h \sim 110\text{--}3000$ pc) and luminosities ($M_V \sim -7$ to -12 mag) largely consistent with Local Group dwarfs. The three new NGC 253 satellites are among the faintest systems discovered beyond the Local Group. We also use archival HI data to place limits on the gas content of our discoveries. Deep imaging surveys such as our program around NGC 253 promise to elucidate the faint end of the satellite luminosity function and its scatter across a range of galaxy masses, morphologies, and environments in the decade to come.

Unified Astronomy Thesaurus concepts: Dwarf galaxies (416); HST photometry (756); Galaxy evolution (594); Galaxies (573); Surveys (1671); Stellar populations (1622)

1. Introduction

Low-mass dwarf galaxies are an important probe at the intersection of the smallest dark matter halos and the astrophysical processes that shape galaxy formation. In the Λ CDM model for structure formation, galaxies grow hierarchically within DM halos, but quantitatively verifying this picture on dwarf galaxy scales has proved challenging (Bullock & Boylan-Kolchin 2017). These challenges include the “missing satellites problem” (e.g., Moore et al. 1999; Klypin et al. 1999), “too big to fail” (e.g., Boylan-Kolchin et al. 2011, 2012), and the apparent planes of satellites around nearby galaxies (e.g., Pawlowski et al. 2012; Ibata et al. 2013; Müller et al. 2018).

Significant progress has been made in addressing these small-scale Λ CDM challenges on the theoretical front, as the inclusion of realistic baryonic physics into simulations of Milky Way–like galaxies can broadly reproduce the properties of the dwarf galaxies in the Local Group (e.g., Brooks et al. 2013; Sawala et al. 2016; Wetzel et al. 2016; Samuel et al. 2021; Engler et al. 2021).

At the same time, the number and diversity of observed satellites around the Milky Way (MW) continue to grow (most recently Mau et al. 2020; Cerny et al. 2021). The MW will remain an essential proving ground for understanding the astrophysics and cosmological implications of the faintest dwarf galaxy satellites because of the detail and depth with which it can be studied (see Simon 2019 for a recent review).

Despite the progress in the Local Group, its detailed study will not be sufficient for verifying the Λ CDM model on small scales, and there is a danger of “overtuning” the models to match local observations alone. Fortunately, in the coming decade we will greatly expand our understanding of faint satellites not just within our own Local Group, but well into the Local Volume to sample primary halos with a range of masses, morphologies, and environments all the way down to the ultra-faint dwarf galaxy scale (e.g., see the recent simulations and discussion in Mutlu-Pakdil et al. 2021). Indeed, the census of faint dwarfs around nearby galaxies is well underway using resolved and unresolved imaging (e.g., Chiboucas et al. 2013; Sand et al. 2014, 2015; Crnojević et al. 2014, 2016b, 2019; Carlin et al. 2016, 2021; Toloba et al. 2016c; Danieli et al. 2017; Smercina et al. 2018; Bennet et al. 2017, 2019, 2020; Carlsten et al. 2021b; Davis et al. 2021; Drlica-Wagner et al. 2021; Carlsten et al. 2021a; Garling et al. 2021), as well as spectroscopic surveys around MW analogs at larger distances (Geha et al. 2017; Mao et al. 2021). These data are already

* This paper includes data gathered with the 6.5 m Magellan Telescope at Las Campanas Observatory, Chile.

yielding new challenges, with simulations of MW-like galaxies showing a higher fraction and number of quiescent satellites with respect to the observations (Karunakaran et al. 2021).

In this work, we present Hubble Space Telescope (HST) observations of dwarf galaxy candidates around NGC 253 ($D \approx 3.5$ Mpc; Radburn-Smith et al. 2011, a total stellar mass of $\approx 4.4 \times 10^{10} M_{\odot}$; Bailin et al. 2011), the principal galaxy of the nearby Sculptor group. These dwarf satellites were discovered as part of the Panoramic Imaging Survey of Centaurus and Sculptor (PISCeS; Sand et al. 2014; Toloba et al. 2016c; Crnojević et al. 2014, 2016b, 2019; Hughes et al. 2021; Mutlu-Pakdil et al. 2021), and include three new discoveries of ultra-faint dwarf satellites (adopting the definition of $M_V \gtrsim -7.7$ in Simon 2019) around NGC 253. In Section 2 we give an overview of PISCeS and the search for satellites around NGC 253, and in Section 3 we present the HST observations of our new NGC 253 dwarf galaxy candidates. In Section 4 we measure the properties of our dwarf sample, including their stellar population, distance, gas content, and structural parameters. We discuss and conclude in Section 5.

2. PISCeS and Discovery of Three Dwarf Satellites Around NGC 253

PISCeS is a Magellan+Megacam survey to search for faint satellites and signs of hierarchical structure formation in the halos of two nearby galaxies of different morphologies in two environments substantially different from the Local Group—the starbursting spiral NGC 253 in a loose group of galaxies ($D \approx 3.5$ Mpc; Radburn-Smith et al. 2011) and the elliptical NGC 5128, or Centaurus A (Cen A) in a relatively rich group ($D \approx 3.8$ Mpc; Harris et al. 2010). The PISCeS campaign has led to the discovery of 11 new satellite candidates around Cen A and several previously unknown streams and shells (Crnojević et al. 2016b), which were later followed up with HST data and confirmed (Crnojević et al. 2019).

As part of PISCeS, we have observed 82 Megacam fields around NGC 253, which reach out to a projected radius of ~ 100 kpc ($\sim 1/3$ of its virial radius; see Figure 1 for the survey footprint). Megacam has a $\sim 24' \times 24'$ field of view (FoV) and a binned pixel scale of $0''.16$. PISCeS typically observes each field for 6×300 s in each of the g and r bands to achieve image depths of $g, r \approx 26.5$ mag, which is ~ 2 magnitudes below the tip of the red giant branch (TRGB) at the distance of NGC 253. The median seeing throughout the survey has been $\sim 0''.8$ in both bands. The data are reduced in a standard way by the Smithsonian Astrophysical Observatory Telescope Data Center (see McLeod et al. 2015; Crnojević et al. 2016b, for further details).

We visually inspect all the images, searching for spatially compact overdensities of stars that have some signs of diffuse light as well. In the early stages of the survey, two faint NGC 253 satellites were reported in Sand et al. (2014; Scl-MM-dw1) and Toloba et al. (2016c; Scl-MM-dw2¹³). Our visual search uncovered three new faint, partially resolved and elongated satellite galaxies, which we dub Scl-MM-dw3, Scl-MM-dw4, and Scl-MM-dw5, in accordance with our prior work in the Sculptor group. During the preparation of this paper, we learned that Martinez-Delgado et al. (2021) reported

the independent discovery of Scl-MM-dw3 (which the authors named Donatiello II) using Dark Energy Survey (DES) data, along with two other faint dwarf candidates outside of the PISCeS footprint (Donatiello III and IV). However, due to the DES depth, the authors could not determine their distance thus could not establish their association with NGC 253. The locations and properties of the NGC 253 dwarfs in the PISCeS footprint are given in Figure 1 and Table 1. In the current work, we focus on the HST color–magnitude diagrams and derived properties of this set of five faint dwarf galaxies. These objects appear to represent a complete sample of the dwarf galaxies detectable in the PISCeS data set; the overall detection efficiency and a satellite luminosity function will be presented in a forthcoming work.

3. HST Observations and Photometry

Including the discoveries of Scl-MM-dw1 and Scl-MM-dw2, PISCeS has uncovered five dwarf satellites around NGC 253 in total (see Table 1). We obtained HST follow-up observations of these dwarfs with the Wide Field Channel (WFC) of the Advanced Camera for Surveys (ACS). Most of the targets were observed as part of the program GO-15938 (PI: Mutlu-Pakdil), with the exception of Scl-MM-dw2, which was observed as part of program GO-14259 (PI: Crnojević). Each target was observed for a total of one orbit (two orbits for Scl-MM-dw2) in the F606W and F814W filters, yielding exposure times of ~ 1100 and 2500 s per filter, for one and two orbits, respectively.

We performed point-spread function photometry on the pipeline-produced FLC images with the latest version (2.0) of DOLPHOT (Dolphin 2000). We followed the recommended preprocessing steps and used the suggested input parameters from the DOLPHOT User Guide.¹⁴ Specifically, we used DOLPHOT parameters recommended for uncrowded fields: FitSky=1, Force1=0, and RAper=4. The initial photometry is culled with the following criteria: the sum of the crowding parameters in the two bands is < 1 , the squared sum of the sharpness parameters in the two bands is < 0.075 , and the signal-to-noise ratio is > 4 and object-type is ≤ 2 in each band. We corrected for Milky Way extinction on a star-by-star basis using the Schlegel et al. (1998) reddening maps with the coefficients from Schlafly & Finkbeiner (2011). The extinction-corrected photometry is used throughout this work.

We performed artificial star tests in order to quantify the photometric uncertainties and completeness in our observations. A total of $\sim 100,000$ artificial stars, implanted one star at a time using the artificial star utilities in DOLPHOT, were distributed uniformly both in color–magnitude space (i.e., $20 \leq F606W \leq 30$ and $0 \leq F606W - F814W \leq 1.5$) and spatially across the field of view. Photometry and quality cuts were performed in an identical manner to those performed on the original photometry. We derived the recovery fractions as a function of magnitude. The 50% (90%) completeness magnitude was determined by the limit where 50% (90%) of artificial stars inserted into the image are successfully recovered by our photometry. Our one-orbit HST data are 50% (90%) complete at F606W ~ 27.1 (26.4) mag and F814W ~ 26.4 (25.7) mag, while the two-orbit data set of Scl-MM-dw2 reaches 50% (90%) completeness at F606W = 27.9 (27.2) mag and F814W = 27.1 (26.6) mag.

¹³ This galaxy was independently discovered by Romanowsky et al. (2016) and was named NGC 253-dw2 in their work.

¹⁴ <http://americano.dolphinim.com/dolphot/dolphotACS.pdf>

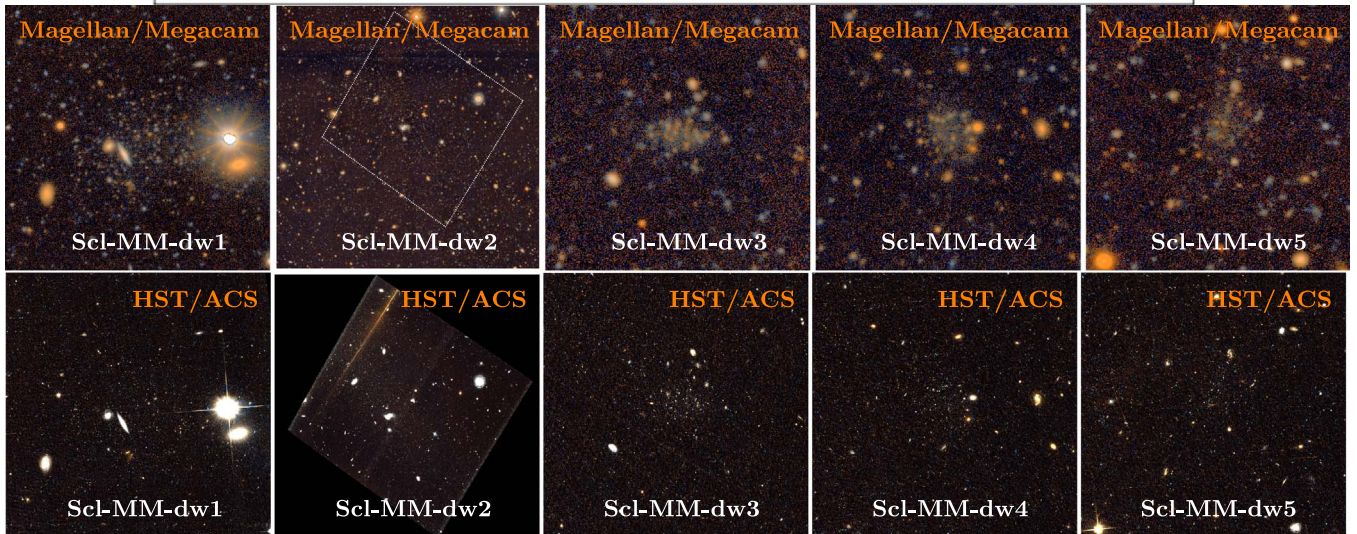
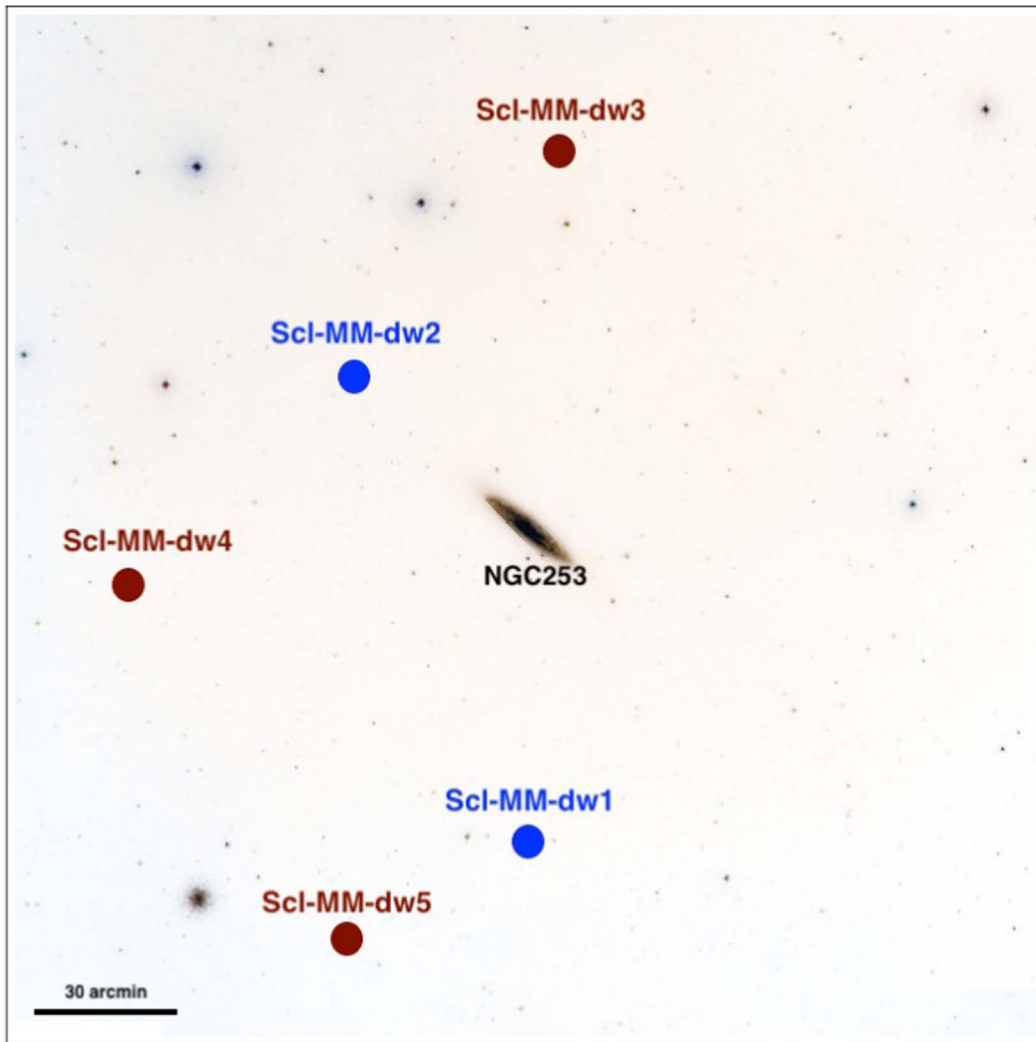


Figure 1. Top panel: DSS image centered on NGC 253, showing the area explored by PISCeS, extending up to 100 kpc from the center. Solid blue circles represent the position of dwarfs previously discovered in PISCeS (Scl-MM-dw1, Sand et al. 2014; Scl-MM-dw2, Toloba et al. 2016c) while red circles represent new dwarf galaxies reported in this study. North is up, and east to the left. Middle (bottom) panel: RGB false color Magellan/Megacam (HST/ACS) images of our dwarf galaxy discoveries. The image cutout sizes of Scl-MM-dw1 are $1'.5 \times 1'.5$. The Megacam cutout size of Scl-MM-dw2 is $6' \times 6'$. The ACS FoV, shown with the white dotted box, is too small to cover the entire body of Scl-MM-dw2 ($r_h = 3.2 \pm 0'.6$), therefore we show the entire ACS FoV for Scl-MM-dw2 in the bottom panel. The size of the other cutouts is $1' \times 1'$. Note that 1 arcmin corresponds to 1.02 kpc at 3.5 Mpc.

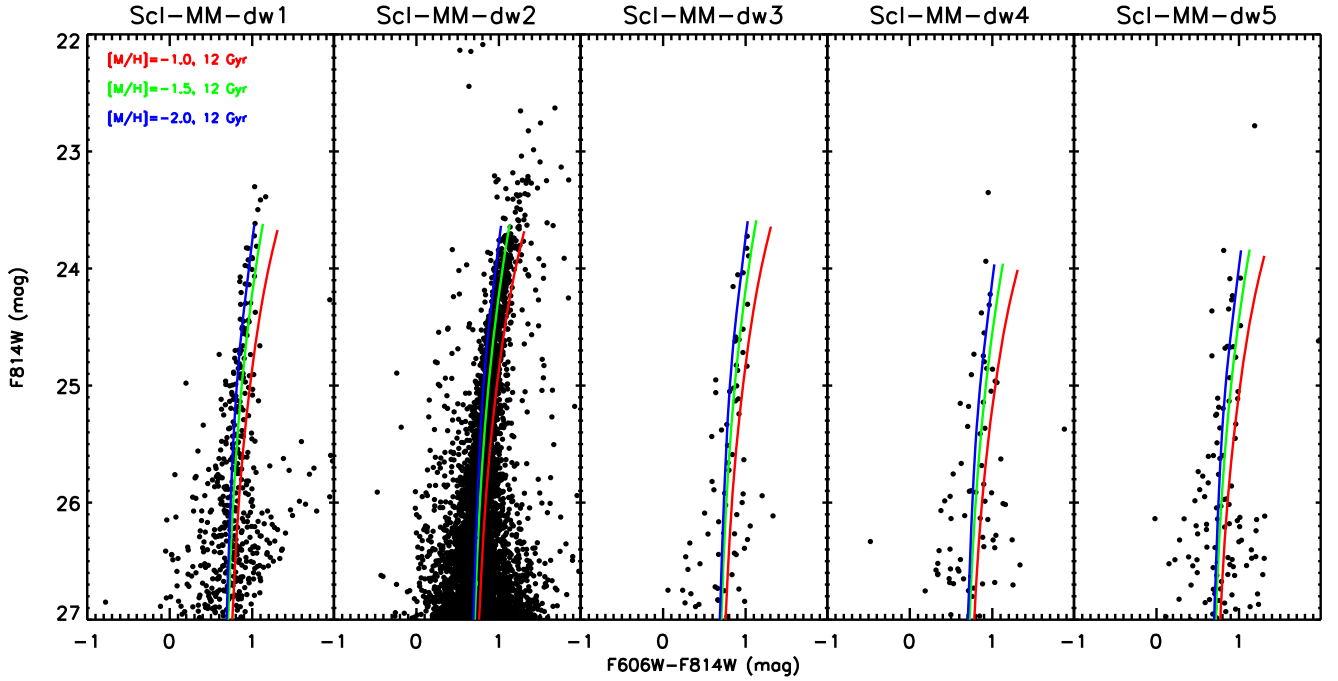


Figure 2. HST CMDs showing the stars within $2 \times r_h$ of each dwarf galaxy except Scl-MM-dw2 (its CMD includes all stars within the ACS FoV, and does not cover the entire body of Scl-MM-dw2, $r_h = 3.2 \pm 0.6$). The blue, cyan, and red lines indicate the PARSEC isochrones for 12 Gyr and $[M/H] = -2.0$ dex, -1.5 dex, and -1.0 dex, respectively. We shift each isochrone by the best-fit distance modulus that we derive in Section 4.2.

Table 1
HST-derived Properties of NGC 253 Dwarfs

Parameter	Scl-MM-dw1	Scl-MM-dw2	Scl-MM-dw3	Scl-MM-dw4	Scl-MM-dw5
R.A. (deg)	$11.89643 \pm 2''0$	$12.57108 \pm 4''0^a$	$11.77950 \pm 1''4$	$13.45476 \pm 1''6$	$12.60776 \pm 1''2$
Decl. (deg)	$-26.38971 \pm 2''0$	$-24.74961 \pm 7''3^a$	$-23.95573 \pm 0''6$	$-25.47442 \pm 1''8$	$-26.72726 \pm 2''5$
$F814W_{\text{TRGB}}$ (mag)	23.72 ± 0.33	23.72 ± 0.03	$23.69^{+0.06}_{-0.15}$	$24.05^{+0.06}_{-0.15}$	$23.94^{+0.08}_{-0.13}$
$m - M$ (mag)	27.73 ± 0.33	27.74 ± 0.07	$27.70^{+0.09}_{-0.18}$	$28.07^{+0.09}_{-0.18}$	$27.95^{+0.10}_{-0.15}$
D (Mpc)	3.53 ± 0.55	3.53 ± 0.11	$3.48^{+0.14}_{-0.28}$	$4.10^{+0.16}_{-0.32}$	$3.90^{+0.18}_{-0.27}$
D_{proj} (kpc)	66	50	81	86	96
M_V (mag)	-8.75 ± 0.11	-12.10 ± 0.50^a	$-7.24^{+0.26}_{-0.21}$	$-7.26^{+0.27}_{-0.23}$	$-7.50^{+0.28}_{-0.20}$
$M_{\text{star}}(M_{\odot})$	$(4.3 \pm 0.5) \times 10^5$	$(0.9^{+0.6}_{-0.3}) \times 10^7$	$(1.1 \pm 0.2) \times 10^5$	$(1.1 \pm 0.3) \times 10^5$	$(1.4 \pm 0.3) \times 10^5$
$\log(M_{\text{HI}}/M_{\odot})$	< 6.5	$< 5.1^a$ ^b	< 6.5	< 6.5	< 6.5
r_h (arcsec)	18.8 ± 1.8	194.4 ± 30.6^a	6.6 ± 1.8	9.5 ± 2.6	19.0 ± 5.2
r_h (pc)	321 ± 31	2940 ± 460^a	111 ± 30	188 ± 51	358 ± 99
ϵ	0.20 ± 0.07	0.66 ± 0.06^a	0.57 ± 0.12	0.43 ± 0.19	0.66 ± 0.11
Position Angle (deg)	133 ± 24	31 ± 3^a	70 ± 13	80 ± 46	169 ± 7

Notes. R.A.: the Right Ascension (J2000.0). Decl.: the Declination (J2000.0). $F814W_{\text{TRGB}}$: TRGB magnitude in F814W. $m - M$: the distance modulus. D : the distance of the galaxy in Mpc. D_{proj} : the projected distance to NGC 253 in kpc. M_V : the absolute V -band magnitude. M_{star} : the stellar mass in solar mass, derived from the measured luminosity by assuming an average $V -$ band mass-to-light of $M_{\text{star}}/L_V = 1.6$ (Woo et al. 2008) appropriate for old stellar populations. $\log(M_{\text{HI}}/M_{\odot})$: 3σ upper limits on the H I mass of each object. r_h : the elliptical half-light radius along the semimajor axis. ϵ : ellipticity is defined as $\epsilon = 1 - b/a$, where b is the semiminor axis and a is the semimajor axis.

^a The values are taken from Toloba et al. (2016c).

^b This value was derived from deep H I observations from the Green Bank Telescope, and it corresponds to 5σ upper limits on the H I mass.

4. Properties of NGC 253 Dwarfs

4.1. Color–Magnitude Diagram

Figure 2 shows the HST color–magnitude diagrams (CMDs) of the five dwarfs, which include stars within two half-light radii (see Table 1 and Section 4.3). Note that the ACS FoV is too small to cover the entire body of Scl-MM-dw2 ($r_h = 3.2 \pm 0.6$ arcmin), therefore we include all stars in the entire ACS FoV for Scl-MM-dw2. Overplotted as blue, cyan, and red lines are the PARSEC

isochrones (Bressan et al. 2012) for 12 Gyr and $[M/H] = -2.0$ dex, -1.5 dex, and -1.0 dex, respectively. Each dwarf is clearly resolved into its constituent red giant branch (RGB) stars in the HST data, and shows old, metal-poor stellar populations at roughly the distance to NGC 253 (see Section 4.2).

Scl-MM-dw3, Scl-MM-dw4, and Scl-MM-dw5 are extremely faint and have sparsely populated RGBs. They are consistent with old, metal-poor systems comprised of predominantly ancient stellar populations, similar to the ultra-faint

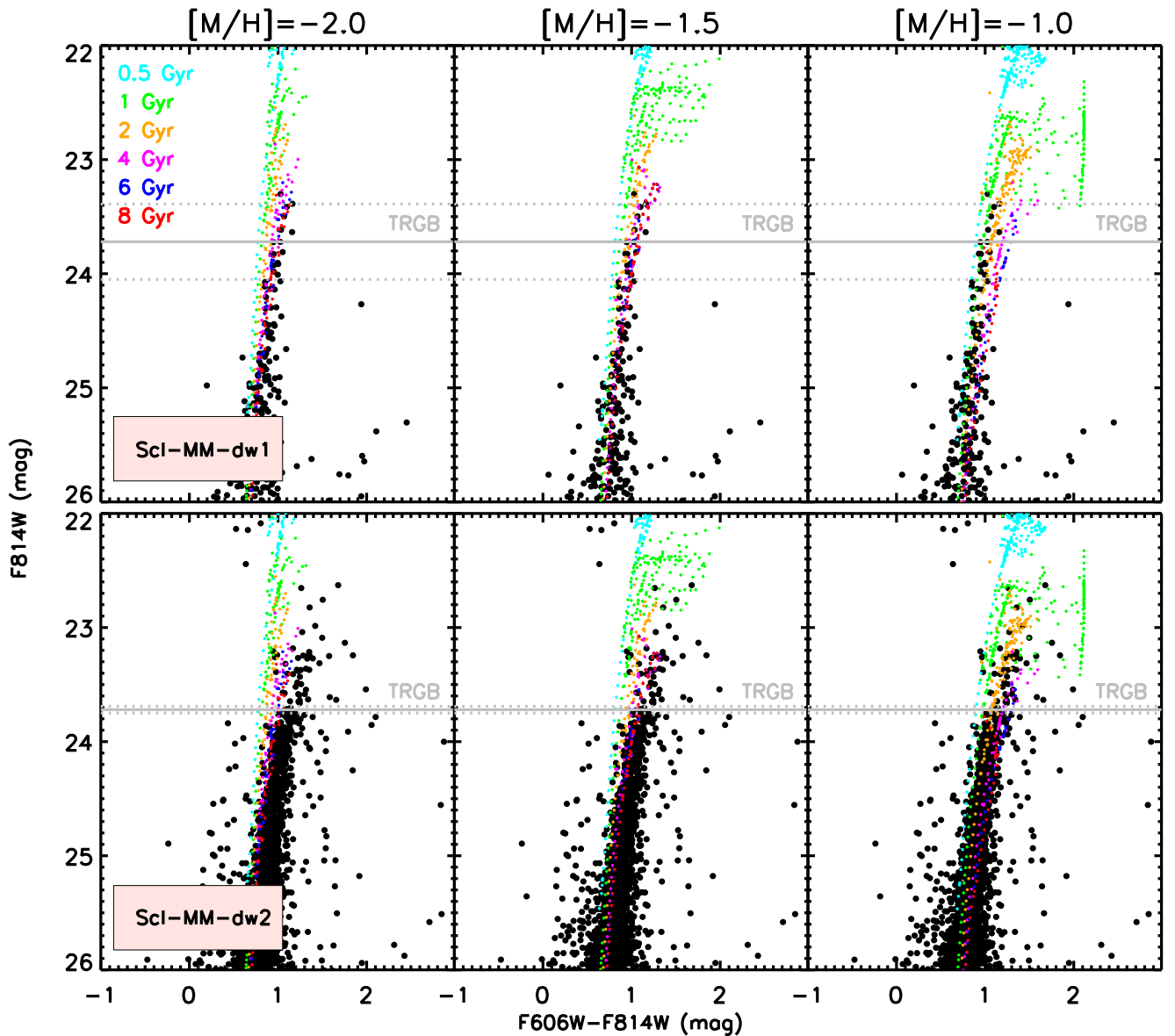


Figure 3. To better understand the AGB stars in Scl-MM-dw1 (top panel) and Scl-MM-dw2 (bottom panel), we plot the AGB phase of PARSEC isochrones for the indicated ages over their stars (black points) for different metallicities (left: $[M/H] = -2$, middle: $[M/H] = -1.5$, right: $[M/H] = -1.0$). The gray horizontal line indicates the best fit for the TRGB, and the dotted lines represent the 1σ uncertainty. We roughly look for a match between the isochrones and stars that are above the TRGB. The match suggests a population of ~ 1 – 2 Gyr and $[M/H] \sim -1.0$ dex for the AGB stars in Scl-MM-dw2, and a population of $\gtrsim 6$ – 8 Gyr for the AGB stars in Scl-MM-dw1.

dwarfs in the MW and M31 (e.g., Brown et al. 2012, 2014; Martin et al. 2016; Simon 2019).

The old RGB in Scl-MM-dw2 closely follows the isochrone of $[M/H] = -1.5$ (green line), which is what we would expect for its luminosity ($M_V = -12.1$) based on the luminosity-metallicity relationship (Kirby et al. 2013). This implies that the stripping of stars in the satellite suggested by Toloba et al. (2016c) should be moderate. However, we note that the relationship has a lot of scatter; and given its large size and elongation, the object is likely undergoing a tidal interaction (see Section 5).

In the ground-based Magellan imaging (Sand et al. 2014; Toloba et al. 2016c), both Scl-MM-dw1 and Scl-MM-dw2 showed some evidence of a younger asymptotic giant branch (AGB) stellar population, which is confirmed by our deeper HST follow-up imaging. Figure 3 shows the AGB phase for isochrones with a range of ages and metallicities for both of

these galaxies. Scl-MM-dw1 seems to contain only a handful of such luminous, possibly intermediate-age populations; these stars complicate its TRGB identification, resulting in a larger uncertainty in the TRGB value ($F814W_{\text{TRGB}} = 23.72 \pm 0.33$ mag, see Section 4.2). This galaxy does not seem to contain populations younger than ~ 6 – 8 Gyr: the low stellar mass of Scl-MM-dw1 and the inherent stochasticity of the AGB phase make it difficult to constrain the amount of possible intermediate-age star formation. In Scl-MM-dw2, the presence of bright AGB stars stretching ~ 1 magnitude above the TRGB requires young populations. The best-fit stellar models suggest these stars are ~ 1 – 2 Gyr old, and are somewhat more metal-rich than the bulk of stars along the RGB. To put constraints on the mass fractions in its younger stars, we use three luminosity functions from the PARSEC library (assuming a Kroupa IMF): one is for a 12 Gyr and $[M/H] = -1.5$ stellar population (see the green isochrone in Figure 2), and others are for a 1 Gyr and

2 Gyr, $[M/H] = -1.0$ stellar population (see Figure 3, bottom-right panel). Then, we explore how much stellar mass at 1–2 Gyr is expected to give the number of stars above the TRGB (53 stars) while producing the number of stars below the TRGB but brighter than $F814W = 25.5 \text{ mag}^{15}$ (1062 stars). We find that $\sim 10\%$ of the stellar mass is in a $\sim 1\text{--}2$ Gyr population.

4.2. Distance

We measure distances to our targets using the TRGB method (e.g., Lee et al. 1993; Salaris et al. 2002; Rizzi et al. 2007), which relies on the fixed luminosity of the core helium ignition stage for old stellar populations (e.g., Serenelli et al. 2017). We first apply a color correction to our photometry, following Jang & Lee (2014; their Formula 5 and Table 6); we then compute the observed luminosity function for RGB stars. The latter is fit with a model luminosity function, which is convolved with the appropriate photometric uncertainty and completeness function as derived from our artificial star tests. More details on the TRGB magnitude recovery method can be found in Crnojević et al. (2019). Our final uncertainties combine in quadrature the fitting uncertainties (which include the artificial star test results), the uncertainties from the TRGB zero-point calibration and the applied color correction, and an assumed uncertainty of 10% on the adopted extinction value. Note that NGC 253 is located at a very high galactic latitude ($b = -88^\circ$) such that the MW star contamination is very low.

The TRGB values, the distance moduli, and the distances for our targets are reported in Table 1. For Scl-MM-dw1 and Scl-MM-dw2, the distances derived from the HST data set are consistent with those derived from the discovery Magellan data set within the uncertainties; the large uncertainty for Scl-MM-dw1 is due to the possible presence of a handful of luminous AGB stars.

For the remaining three dwarfs, the paucity of RGB stars prevented the code from converging to a reasonable result (as already described in, e.g., Carlin et al. 2021). We thus apply a simple Sobel filter edge-detection algorithm to these dwarfs (following the prescription from Sakai et al. 1996), and computed the related uncertainties with a Monte Carlo (MC) calculation, varying the position of the stars in the CMD within their photometric errors. However, for our three faint dwarfs, it seems likely that the shot noise in the CMD is a larger effect than the photometric uncertainties. To simulate the shot noise, we first produce a well-populated CMD (of $\sim 20,000$ stars) in HST filters, including our completeness and photometric uncertainties, by using an old, metal-poor isochrone (12 Gyr, $[M/H] = -2.0$ dex) and its associated luminosity function. We then randomly select the observed number of stars from this artificial CMD and measure the typical offset between the brightest simulated star and the location of the TRGB via 1000 realizations. We find that the offset is 0.09 mag for a faint system like Scl-MM-dw3 or Scl-MM-dw4 ($M_V \sim -7.25$, see Table 1 and Section 4.4), and 0.05 mag for a Scl-MM-dw5-like dwarf ($M_V = -7.50$), while the offset is consistent with zero for a Scl-MM-dw1-like dwarf ($M_V = -8.75$). This clearly shows that the TRGB technique alone is no longer reliable for ultra-faint dwarfs, and the shot noise should be properly accounted for at these magnitudes. We add these offsets to our bright-end of the MC uncertainties as the

measured TRGB will always be below the true TRGB because of the paucity of RGB stars in the faint dwarfs.

The good agreement of TRGB distances with the distance of NGC 253 (e.g., Radburn-Smith et al. 2011, who found $m - M = 27.70 \pm 0.07$) firmly establishes their membership with NGC 253.

4.3. Structural Properties

We derive structural parameters (including half-light radius r_h , ellipticity, and position angle) for the dwarfs using the maximum-likelihood (ML) method of Martin et al. (2008), as implemented by Sand et al. (2009). In our analysis, we select stars consistent with an old, metal-poor isochrone in color–magnitude space after taking into account photometric uncertainties, within our 90% completeness limit. We inflate the uncertainty to 0.1 mag when the photometric errors are < 0.1 mag for the purpose of selecting stars to go into our ML analysis. The stellar profiles of the dwarfs are generally well described by a single exponential model (e.g., Martin et al. 2008; Muñoz et al. 2018). We fit a standard exponential profile plus constant background to the data and summarize the resulting structural parameters in Table 1. The quoted r_h is the best-fit elliptical half-light radius along the semimajor axis. Uncertainties are determined by bootstrap resampling the data 1000 times and recalculating the structural parameters for each resample. We check our results by repeating the calculations with the same set of stars, but with a limit of one magnitude fainter. The derived structural parameters using both samples are consistent within the uncertainties.

Our results for Scl-MM-dw1 are in good agreement with those derived from Magellan+Megacam imaging (Sand et al. 2014): we find $r_h = 18''.8 \pm 1''.8$ with an ellipticity of 0.20 ± 0.07 while their value is $16''.8 \pm 2''.4$ with an ellipticity of < 0.42 . Compared to the structural parameters derived with integrated light from DES data ($r_h = 5''.5 \pm 0''.4$, $\epsilon = 0.39 \pm 0.04$, Martinez-Delgado et al. 2021), our ML analysis for Scl-MM-dw3 suggests a similar size ($r_h = 6''.6 \pm 1''.8$) and a more elongated shape ($\epsilon = 0.57 \pm 0.12$). Due to its large physical size ($r_h = 3''.2 \pm 0''.5$, 2.9 ± 0.5 kpc), the HST FoV is too small to derive robust structural parameters of Scl-MM-dw2. Therefore, we adopt the results from our Magellan+Megacam imaging (Toloba et al. 2016c) and do not attempt to revisit its structural parameters here.

4.4. Luminosity

We derive absolute magnitudes for our objects by using the same procedure as in Mutlu-Pakdil et al. (2018), as was first described in Martin et al. (2008). First, we produce a well-populated CMD (of $\sim 20,000$ stars) in HST filters, including our completeness and photometric uncertainties, by using the PARSEC isochrone with age 12 Gyr and $[M/H] = -2.0$ dex and its associated luminosity function assuming a Kroupa IMF (Kroupa 2001). Using one with $[M/H] = -1.5$ dex or $[M/H] = -2.5$ dex gives a result consistent within the uncertainties (see Section 3 in Martin et al. 2008 for a detailed discussion on uncertainties). We then randomly select the same number of stars from this artificial CMD as was found from our profile fits. We obtain the total luminosity by summing the flux of these stars and extrapolating the flux of the faint, unresolved component of the galaxy from the adopted luminosity function. We calculate 1000 realizations in this way and take the mean as our absolute magnitude and its standard deviation as the uncertainty. To

¹⁵ We choose a magnitude brighter than our 90% completeness limit for Scl-MM-dw2 to make sure incompleteness is not a concern.

account for the uncertainty on the number of stars (assuming Poisson statistics), we repeat this operation 100 times, varying the number of stars within its uncertainty, and use the offset from the best-fit value as the associated uncertainty. These error terms and the distance modulus uncertainty are then added in quadrature to produce our final uncertainty on the absolute magnitude. The final values can be found in Table 1.

Our HST-based luminosity measurement gives a fainter value for Scl-MM-dw1 ($M_V = -8.75 \pm 0.11$ versus the Magellan-based luminosity of $M_V = -10.3 \pm 0.6$; Sand et al. 2014). It is worth noting that the Magellan-based luminosity was derived using a large aperture around the extent of the dwarf, and the existence of a bright star and several background galaxies in the vicinity of Scl-MM-dw1 (see Figure 1) appears to be the reason for a brighter result in the ground-based data. For Scl-MM-dw3, our luminosity measurement ($M_V = -7.24 \pm 0.21$) is consistent with the one reported in Martinez-Delgado et al. (2021, $M_V = -7.04 \pm 0.2$), within the uncertainties. For Scl-MM-dw2, similar to its structural parameters, we opt to use the Magellan-based luminosity ($M_V = -12.1 \pm 0.5$, Toloba et al. 2016c) due to its large physical size and the small ACS FoV.

4.5. HI Gas Limits

Sand et al. (2014) used data from the HIParkes All-Sky Survey (HIPASS; Barnes et al. 2001) to constrain the HI content of Scl-MM-dw1, with no detection, and a 3σ HI gas mass upper limit of $\log(M_{\text{HI}}/M_\odot) \lesssim 6.5$. Likewise, Toloba et al. (2016c) first checked the HIPASS spectra for Scl-MM-dw2, and found a tentative $\sim 3.7\sigma$ HI emission peak along its line of sight. However, the authors later obtained much deeper HI observations on the Green Bank Telescope, and did not detect any HI gas in emission, which constrains the gas mass of Scl-MM-dw2 to a 5σ upper limit of $\log(M_{\text{HI}}/M_\odot) < 5.1$ (Toloba et al. 2016c).

Similarly, we investigate the possibility of HI gas associated with our three discoveries by using the HIPASS data, and find no evidence of a detection in any of them. The typical noise in these spectra is $18 \text{ mJy in } 13.2 \text{ km s}^{-1}$ channels. That gives a 3σ flux limit, assuming any real source would span 2 channels, of 1 Jy km s^{-1} . Converting this to an HI mass limit gives us a 3σ HI gas mass upper limit of $\log(M_{\text{HI}}/M_\odot) \lesssim 6.5$ (see Table 1). This limit is consistent with the dwarfs being gas-poor, similar to other faint Local Volume dwarf satellites that reside within the virial radius of their primary galaxy (e.g., Grcevich & Putman 2009; Spekkens et al. 2014; Karunakaran et al. 2020). However, given their low stellar masses, their gas content would not be detectable even if it was relatively high.

5. Discussion and Conclusions

In dedicated deep surveys with accompanying HST imaging, only a handful of distant ultra-faint dwarfs have been discovered and studied in detail with accurate distance information, e.g., Virgo UFD1 ($M_V = -6.5$; Jang & Lee 2014, far from any massive galaxies) in the Virgo cluster, MADCASH1 ($M_V = -7.8$; Carlin et al. 2016, 2021) around NGC 2403 (a relatively isolated galaxy with a stellar mass similar to the Large Magellanic Cloud), and Fornax UFD1 ($M_V = -7.6$; Lee et al. 2017) in the outskirts of NGC 1316, a giant elliptical galaxy in the Fornax cluster. Therefore, the sample of ultra-faints beyond the Local Group is still too small and heterogeneous for comparative studies. As little is known about the ultra-faints outside the Local Group, it is

crucial to push the dwarf discovery limit in the Local Volume to the ultra-faint dwarf regime and study them in detail.

In this work, we report the discovery¹⁶ of three ultra-faint dwarf satellite galaxies of NGC 253 in a visual search of the Magellan/Megacam images taken as part of PISCeS, our panoramic imaging campaign to find faint substructure within $\lesssim 100 \text{ kpc}$ of NGC 253. This brings the total number of NGC 253 satellites uncovered by PISCeS to five. We present HST follow-up of these five dwarfs, confirm their nature, and firmly establish their membership with NGC 253 by deriving TRGB distances.

We estimate the structural parameters and luminosities of NGC 253 dwarfs and compare them with those of the Local Group dwarfs as well as Cen A dwarfs from our own PISCeS program, and with the ultra-diffuse galaxies in the Virgo and Coma clusters (see Figure 4). They are all comparable to MW and M31 dwarf galaxies. However, Scl-MM-dw2 is a slight outlier: it is one of the most extended and least dense objects known at its luminosity. It is similar to Sagittarius in the Local Group and the recently discovered diffuse Virgo galaxies. It is likely undergoing a tidal interaction (see discussion in Toloba et al. 2016c), as it has a high ellipticity ($\epsilon \approx 0.66$) and is elongated in the direction of NGC 253.

Our luminosity measurement places Scl-MM-dw1's luminosity near the faint end of those of the classical dSphs in the MW and M31. The MW satellite most similar to Scl-MM-dw1 is Draco ($M_V = -8.8 \pm 0.3 \text{ mag}$; $r_h = 221 \pm 26 \text{ pc}$; $\epsilon = 0.31 \pm 0.02$, McConnachie 2012). Scl-MM-dw3, Scl-MM-dw4, and Scl-MM-dw5 are well within the ultra-faint dwarf regime ($M_V \gtrsim -7.7$; Simon 2019) in the size–luminosity plane. Their structural parameters and luminosities are comparable to MW ultra-faint dwarf Eridanus II ($M_V = -7.1 \pm 0.3 \text{ mag}$; $r_h = 277 \pm 14 \text{ pc}$; $\epsilon = 0.48 \pm 0.04$, Crmojević et al. 2016a). They are among the faintest dwarf satellites identified beyond the Local Group via a systematic search, demonstrating the effectiveness of PISCeS in extending the faint end of the satellite luminosity function for NGC 253.

The five PISCeS dwarfs are all mostly old and metal-poor stellar systems (age $\sim 12 \text{ Gyr}$; $[M/H] \lesssim -1.5 \text{ dex}$). This is not surprising especially for our three ultra-faint dwarfs: the ultra-faint dwarfs are uniformly old, with nearly all of their stars forming in the early universe, thus considered as pristine fossils from the era of reionization (e.g., Salvadori & Ferrara 2009; Bovill & Ricotti 2011; Brook et al. 2014; Brown et al. 2014). Also, dwarf satellites within $\sim 100 \text{ kpc}$ of their primary galaxy are highly susceptible to loss of their cold gas through tidal or gas dynamical interactions (e.g., Grebel et al. 2003; Mayer et al. 2006). Our nondetection in HIPASS is consistent with this picture.

Compared to our ultra-faint dwarfs, the stellar populations of Scl-MM-dw1 and Scl-MM-dw2 are relatively complex with some evidence of AGB stars. While Scl-MM-dw1 has a handful of AGB consistent with a population of $\gtrsim 6\text{--}8 \text{ Gyr}$, Scl-MM-dw2 shows a clear population of AGB stars that are $\sim 1\text{--}2 \text{ Gyr}$ old with $[M/H] \sim -1.0 \text{ dex}$. Unfortunately, the small HST FoV prevents us from exploring further any trends in the spatial distribution of RGB and AGB stars in Scl-MM-dw2.

Martinez-Delgado et al. (2021) recently performed a visual NGC 253 satellite search using the DES data, and reported three new dwarf candidates, one of which is the same object we

¹⁶ We note Martinez-Delgado et al. (2021) published the independent discovery of one of our objects.

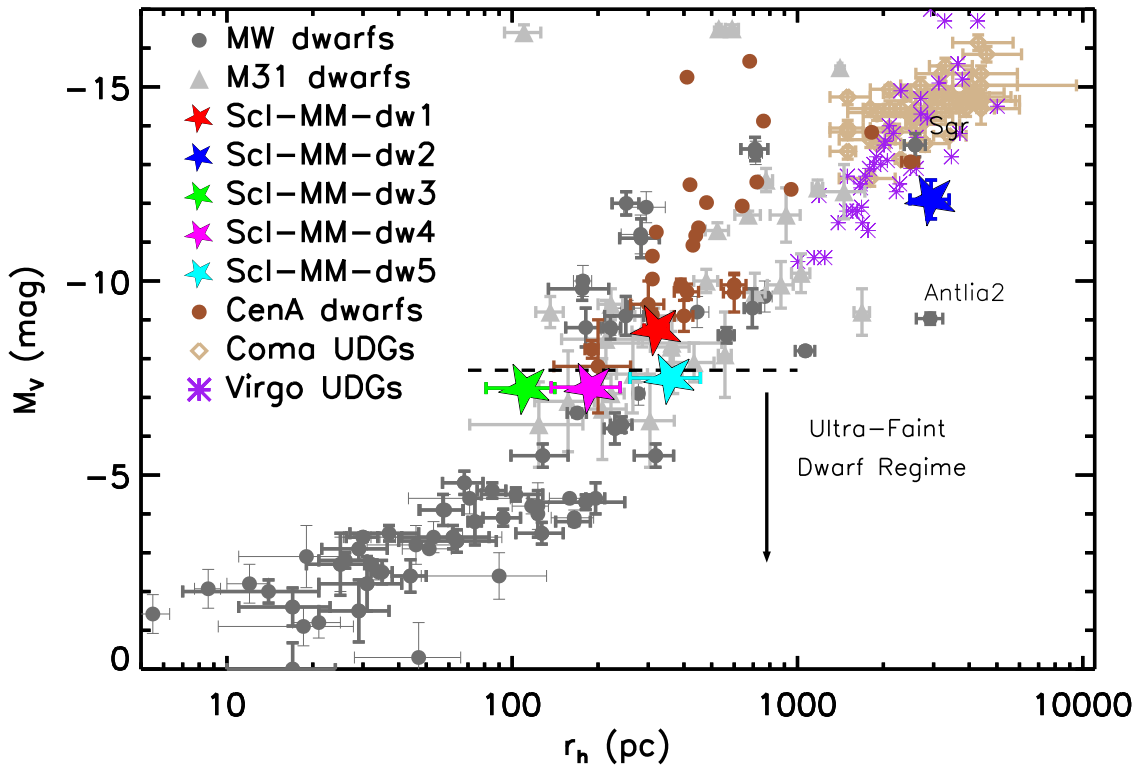


Figure 4. Absolute V -band magnitude as a function of half-light radius for NGC 253 dwarfs, relative to MW/M31 dwarf galaxies, Cen A dwarfs (Sharina et al. 2008; Crnojević et al. 2019), and the faint, diffuse galaxies found in Virgo and Coma by Lim et al. (2020) and van Dokkum et al. (2015), respectively. The newly discovered NGC 253 dwarfs have similar properties to those of LG dwarfs. Scl-MM-dw2 is a slight outlier with a large half-light radius and low surface brightness for its absolute magnitude, similarly to Sagittarius in the Local Group and the recently discovered diffuse Virgo galaxies. The new NGC 253 satellites are among the faintest systems discovered beyond the Local Group.

independently discovered and named as Scl-MM-dw3. The other two are located outside our PISCeS footprint, and their discoveries suggest that there might be more satellites to be discovered at larger radii from NGC 253. Moreover, the authors suggested the possible existence of a spatially flattened and velocity-correlated satellite galaxy system around NGC 253, which might point to an infalling filament or tidal origin. This flattened structure is 31 ± 5 kpc thick (i.e., thickness is here defined as the rms height from the best-fit plane) with the minor-to-major axis ratio of 0.14 ± 0.03 , therefore comparable to the satellite planes found around the MW and M 31 (e.g., Pawlowski & Kroupa 2013; Ibata et al. 2013). Roughly $\sim 30\%$ of our survey footprint falls on this proposed linear structure, and 4 of our 5 dwarfs are consistent with lying along this plane. Follow-up velocities of these dwarf galaxies (e.g., Toloba et al. 2016a, 2016b) will further elucidate the substructure properties of NGC 253 and the Sculptor group.

We conclude by highlighting the crucial role played by PISCeS in identifying ultra-faint dwarf galaxies beyond the Local Group. A future paper will be dedicated to our overall satellite detection efficiency and the luminosity function of NGC 253. This will provide a unique opportunity to study the faint end of the satellite luminosity function in a new, more isolated environment than the Local Group.

We are grateful to P. Bennet for the useful discussions and tabulated data that were used in this paper. We also thank Annika Peter for the useful comments.

Based on observations made with the NASA/ESA Hubble Space Telescope, obtained at the Space Telescope Science Institute, which is operated by the Association of Universities for Research in Astronomy, Inc., under NASA contract NAS5-

26555. All the HST data used in this paper can be found in MAST. These observations are associated with program # HST-GO-15938. Support for program # HST-GO-15938 and HST-GO-14259 was provided by NASA through a grant from the Space Telescope Science Institute, which is operated by the Association of Universities for Research in Astronomy, Inc., under NASA contract NAS5-26555. The Parkes telescope is part of the Australia Telescope which is funded by the Commonwealth of Australia for operation as a National Facility managed by CSIRO.

B.M.P. is supported by an NSF Astronomy and Astrophysics Postdoctoral Fellowship under award AST-2001663. D.J.S. acknowledges support from NSF grants AST-1821967 and 1813708. Research by D.C. is supported by NSF grant AST-1814208. J.D.S. acknowledges support from NSF grant AST-1412792. J.S. acknowledges support from NSF grant AST-1812856 and the Packard Foundation. K.S. acknowledges support from the Natural Sciences and Engineering Research Council of Canada (NSERC).

Facilities: Magellan:Clay (Megacam), HST (ACS), GALEX, Parkes.

Software: Astropy (Astropy Collaboration et al. 2013, 2018), The IDL Astronomy User’s Library (Landsman 1993), DOLPHOT (Dolphin 2000).

ORCID iDs

Burçin Mutlu-Pakdil <https://orcid.org/0000-0001-9649-4815>
 David J. Sand <https://orcid.org/0000-0003-4102-380X>
 Denija Crnojević <https://orcid.org/0000-0002-1763-4128>
 Michael G. Jones <https://orcid.org/0000-0002-5434-4904>

Nelson Caldwell  <https://orcid.org/0000-0003-2352-3202>
 Puragra Guhathakurta  <https://orcid.org/0000-0001-8867-4234>
 Anil C. Seth  <https://orcid.org/0000-0003-0248-5470>
 Joshua D. Simon  <https://orcid.org/0000-0002-4733-4994>
 Kristine Spekkens  <https://orcid.org/0000-0002-0956-7949>
 Jay Strader  <https://orcid.org/0000-0002-1468-9668>
 Elisa Toloba  <https://orcid.org/0000-0001-6443-5570>

References

- Astropy Collaboration, Price-Whelan, A. M., Sipőcz, B. M., et al. 2018, *AJ*, **156**, 123
- Astropy Collaboration, Robitaille, T. P., Tollerud, E. J., et al. 2013, *A&A*, **558**, A33
- Bailin, J., Bell, E. F., Chappell, S. N., Radburn-Smith, D. J., & de Jong, R. S. 2011, *ApJ*, **736**, 24
- Barnes, D. G., Staveley-Smith, L., de Blok, W. J. G., et al. 2001, *MNRAS*, **322**, 486
- Bennet, P., Sand, D. J., Crnojević, D., et al. 2017, *ApJ*, **850**, 109
- Bennet, P., Sand, D. J., Crnojević, D., et al. 2019, *ApJ*, **885**, 153
- Bennet, P., Sand, D. J., Crnojević, D., et al. 2020, *ApJL*, **893**, L9
- Bovill, M. S., & Ricotti, M. 2011, *ApJ*, **741**, 18
- Boylan-Kolchin, M., Bullock, J. S., & Kaplinghat, M. 2011, *MNRAS*, **415**, L40
- Boylan-Kolchin, M., Bullock, J. S., & Kaplinghat, M. 2012, *MNRAS*, **422**, 1203
- Bressan, A., Marigo, P., Girardi, L., et al. 2012, *MNRAS*, **427**, 127
- Brook, C. B., Di Cintio, A., Knebe, A., et al. 2014, *ApJL*, **784**, L14
- Brooks, A. M., Kuhlen, M., Zolotov, A., & Hooper, D. 2013, *ApJ*, **765**, 22
- Brown, T. M., Tumlinson, J., Geha, M., et al. 2012, *ApJL*, **753**, L21
- Brown, T. M., Tumlinson, J., Geha, M., et al. 2014, *ApJ*, **796**, 91
- Bullock, J. S., & Boylan-Kolchin, M. 2017, *ARA&A*, **55**, 343
- Carlin, J. L., Mutlu-Pakdil, B., Crnojević, D., et al. 2021, *ApJ*, **909**, 211
- Carlin, J. L., Sand, D. J., Price, P., et al. 2016, *ApJL*, **828**, L5
- Carlsten, S. G., Greene, J. E., Greco, J. P., Beaton, R. L., & Kado-Fong, E. 2021a, *ApJ*, **922**, 267
- Carlsten, S. G., Greene, J. E., Peter, A. H. G., Beaton, R. L., & Greco, J. P. 2021b, *ApJ*, **908**, 109
- Cerny, W., Pace, A. B., Drlica-Wagner, A., et al. 2021, *ApJ*, **910**, 18
- Chiboucas, K., Jacobs, B. A., Tully, R. B., & Karachentsev, I. D. 2013, *AJ*, **146**, 126
- Crnojević, D., Sand, D. J., Bennet, P., et al. 2019, *ApJ*, **872**, 80
- Crnojević, D., Sand, D. J., Caldwell, N., et al. 2014, *ApJL*, **795**, L35
- Crnojević, D., Sand, D. J., Zaritsky, D., et al. 2016a, *ApJL*, **824**, L14
- Crnojević, D., Sand, D. J., Spekkens, K., et al. 2016b, *ApJ*, **823**, 19
- Danieli, S., van Dokkum, P., Merritt, A., et al. 2017, *ApJ*, **837**, 136
- Davis, A. B., Nierenberg, A. M., Peter, A. H. G., et al. 2021, *MNRAS*, **500**, 3854
- Dolphin, A. E. 2000, *PASP*, **112**, 1383
- Drlica-Wagner, A., Carlin, J. L., Nidever, D. L., et al. 2021, *ApJS*, **256**, 2
- Engler, C., Pillepich, A., Pasquali, A., et al. 2021, *MNRAS*, **507**, 4211
- Garling, C. T., Peter, A. H. G., Kochanek, C. S., Sand, D. J., & Crnojević, D. 2021, *MNRAS*, **507**, 4764
- Geha, M., Wechsler, R. H., Mao, Y.-Y., et al. 2017, *ApJ*, **847**, 4
- Greivich, J., & Putman, M. E. 2009, *ApJ*, **696**, 385
- Grebel, E. K., Gallagher, J. S. I., & Harbeck, D. 2003, *AJ*, **125**, 1926
- Harris, G. L. H., Rejkuba, M., & Harris, W. E. 2010, *PASA*, **27**, 457
- Hughes, A. K., Sand, D. J., Seth, A., et al. 2021, *ApJ*, **914**, 16
- Ibata, R. A., Lewis, G. F., Conn, A. R., et al. 2013, *Natur*, **493**, 62
- Jang, I. S., & Lee, M. G. 2014, *ApJL*, **795**, L6
- Karunakaran, A., Spekkens, K., Bennet, P., et al. 2020, *AJ*, **159**, 37
- Karunakaran, A., Spekkens, K., Oman, K. A., et al. 2021, *ApJL*, **916**, L19
- Kirby, E. N., Cohen, J. G., Guhathakurta, P., et al. 2013, *ApJ*, **779**, 102
- Klypin, A., Kravtsov, A. V., Valenzuela, O., & Prada, F. 1999, *ApJ*, **522**, 82
- Kroupa, P. 2001, *MNRAS*, **322**, 231
- Landsman, W. B. 1993, in ASP Conf. Ser., 52, *Astronomical Data Analysis Software and Systems II*, ed. R. J. Hanisch, R. J. V. Brissenden, & J. Barnes (San Francisco, CA: ASP), 246
- Lee, M. G., Freedman, W. L., & Madore, B. F. 1993, *ApJ*, **417**, 553
- Lee, M. G., Jang, I. S., Beaton, R., et al. 2017, *ApJL*, **835**, L27
- Lim, S., Côté, P., Peng, E. W., et al. 2020, *ApJ*, **899**, 69
- Mao, Y.-Y., Geha, M., Wechsler, R. H., et al. 2021, *ApJ*, **907**, 85
- Martin, N. F., de Jong, J. T. A., & Rix, H.-W. 2008, *ApJ*, **684**, 1075
- Martin, N. F., Ibata, R. A., Lewis, G. F., et al. 2016, *ApJ*, **833**, 167
- Martinez-Delgado, D., Makarov, D., Javanmardi, B., et al. 2021, *A&A*, **652**, A48
- Mau, S., Cerny, W., Pace, A. B., et al. 2020, *ApJ*, **890**, 136
- Mayer, L., Mastroiandro, C., Wadsley, J., Stadel, J., & Moore, B. 2006, *MNRAS*, **369**, 1021
- McConnachie, A. W. 2012, *AJ*, **144**, 4
- McLeod, B., Geary, J., Conroy, M., et al. 2015, *PASP*, **127**, 366
- Moore, B., Ghigna, S., Governato, F., et al. 1999, *ApJL*, **524**, L19
- Müller, O., Pawłowski, M. S., Jerjen, H., & Lelli, F. 2018, *Sci*, **359**, 534
- Muñoz, R. R., Côté, P., Santana, F. A., et al. 2018, *ApJ*, **860**, 66
- Mutlu-Pakdil, B., Sand, D. J., Carlin, J. L., et al. 2018, *ApJ*, **863**, 25
- Mutlu-Pakdil, B., Sand, D. J., Crnojević, D., et al. 2021, *A&J*, **918**, 88
- Pawłowski, M. S., & Kroupa, P. 2013, *MNRAS*, **435**, 2116
- Pawłowski, M. S., Pflamm-Altenburg, J., & Kroupa, P. 2012, *MNRAS*, **423**, 1109
- Radburn-Smith, D. J., de Jong, R. S., Seth, A. C., et al. 2011, *ApJS*, **195**, 18
- Rizzi, L., Tully, R. B., Makarov, D., et al. 2007, *ApJ*, **661**, 815
- Romanowsky, A. J., Martínez-Delgado, D., Martin, N. F., et al. 2016, *MNRAS*, **457**, L103
- Sakai, S., Madore, B. F., & Freedman, W. L. 1996, *ApJ*, **461**, 713
- Salaris, M., Cassisi, S., & Weiss, A. 2002, *PASP*, **114**, 375
- Salvadori, S., & Ferrara, A. 2009, *MNRAS*, **395**, L6
- Samuel, J., Wetzel, A., Chapman, S., et al. 2021, *MNRAS*, **504**, 1379
- Sand, D. J., Crnojević, D., Strader, J., et al. 2014, *ApJL*, **793**, L7
- Sand, D. J., Olszewski, E. W., Willman, B., et al. 2009, *ApJ*, **704**, 898
- Sand, D. J., Spekkens, K., Crnojević, D., et al. 2015, *ApJL*, **812**, L13
- Sawala, T., Frenk, C. S., Fattahi, A., et al. 2016, *MNRAS*, **457**, 1931
- Schlafly, E. F., & Finkbeiner, D. P. 2011, *ApJ*, **737**, 103
- Schlegel, D. J., Finkbeiner, D. P., & Davis, M. 1998, *ApJ*, **500**, 525
- Serenelli, A., Weiss, A., Cassisi, S., Salaris, M., & Pietrinfermi, A. 2017, *A&A*, **606**, A33
- Sharina, M. E., Karachentsev, I. D., Dolphin, A. E., et al. 2008, *MNRAS*, **384**, 1544
- Simon, J. D. 2019, *ARA&A*, **57**, 375
- Smercina, A., Bell, E. F., Price, P. A., et al. 2018, *ApJ*, **863**, 152
- Spekkens, K., Urbancic, N., Mason, B. S., Willman, B., & Aguirre, J. E. 2014, *ApJL*, **795**, L5
- Toloba, E., Guhathakurta, P., Romanowsky, A. J., et al. 2016a, *ApJ*, **824**, 35
- Toloba, E., Sand, D., Guhathakurta, P., et al. 2016b, *ApJL*, **830**, L21
- Toloba, E., Sand, D. J., Spekkens, K., et al. 2016c, *ApJL*, **816**, L5
- van Dokkum, P. G., Abraham, R., Merritt, A., et al. 2015, *ApJL*, **798**, L45
- Wetzel, A. R., Hopkins, P. F., Kim, J.-h., et al. 2016, *ApJL*, **827**, L23
- Woo, J., Courteau, S., & Dekel, A. 2008, *MNRAS*, **390**, 1453